Geomechanics and Engineering, *Vol. 25, No. 6 (2021) 481-493*
DOI: https://doi.org/10.12989/gae.2021.25.6.481

Fracture response and mechanisms of brittle rock with different numbers of openings under uniaxial loading

Hao Wu[1a], Dan Ma[*1], A.J.S. Spearing[1a] and Guoyan Zhao[2a]

[1]School of Mines, China University of Mining and Technology, Xuzhou 221116, China
[2]School of Resources and Safety Engineering, Central South University, Changsha 410083, China

(Received December 22, 2020, Revised May 20, 2021, Accepted June 12, 2021)

Abstract. Hazardous failure phenomena such as rock bursts and slabbing failure frequently occur in deep hardrock tunnels, thus understanding the failure phenomena and mechanisms of the stress regime on tunnels is extremely critical. In this study, the tunnel system in a rock mass was physically modelled as a number of scaled openings in rock specimens, and the mechanical behavior of specimens having one to four horseshoe-shaped openings under uniaxial compression were investigated systematically. During the tests, the digital image correlation (DIC) and acoustic emission (AE) techniques were jointly employed to monitor the fracture response of specimens. After which, the stress distributions in the specimens were numerically analyzed and the stress concentration factor on the periphery of the opening was calculated. The results show that the number of openings have a significant impact on the weakening effect of rock mechanical properties. The progressive cracking process of the specimens with openings evolves from first-tensile cracks through second-tensile cracks and spalling cracks to shear cracks, and the crack threshold stresses are measured. Two failure modes are formed: shear failure and shear-tensile failure. According to the stress distribution law around the opening, the crack initiation mechanism can be fully explained. This research provides an insight to failure mechanism of hardrock tunnel.

Keywords: hardrock tunnel; fracture behavior; failure mechanism; digital image correlation; acoustic emission; stress distribution

1. Introduction

Mankind makes use of an increasing amount of underground space for applications such as mines, roads and railways, parking facilities and water tunnels (La and Kim 2020, Zerhouny *et al.* 2018, Ma *et al.* 2020). The layout of the tunnel system in rock engineering is diverse, including parallel and intersecting tunnels. Thus, the failure mechanisms of the tunnels are quite complicated due to their interaction. Additionally, natural rocks are usually distributed with holes that vary from small-scale pores to large-scale caves, and the stability is noticeably weaker at the holes. According to the theory of elasticity the homogeneity, continuity and isotropy of hard rock mass are generally good, the excavated tunnels and embedded holes in rock masses can be simplified as openings in rock specimens. The study of the mechanical responses of brittle rocks containing openings under stresses is obviously important to understand the failure behavior and the support method needed to ensure stability. In mining this is further complicated because the stress regime around an excavation changes as mining progresses.

As the excavation depth increases, the frequency of rock disasters increases in hard rock tunnels (Lee *et al.* 2020a, Wagner 2017, Dang *et al.* 2019, Ma *et al.* 2021). Inspired by the V-shaped notch formation and rock bursts appearing on the hardrock tunnel sidewalls, Hoek (1965) first performed an experimental investigation on prismatic Columbia resin models having a single circular opening under biaxial compression with low confinement employing a photo elastic method. He observed three types of cracks (primary fracture, remote fracture and sidewall fracture) appearing around the opening. This phenomenon has also been found in rock specimens (Martin 1993), with the increase of the confining pressure, the tensile cracks are gradually suppressed and are no longer evident whilst the sidewall failure becomes more and more severe (Wang *et al.* 2012). Wong *et al.* (2006) systematically analyzed the influence of specimen width and opening size on splitting failure behavior of granite containing a circular opening under uniaxial loading. They summarized the primary tensile cracks propagate more easily in narrow specimens with large openings. Afterwards, Sammis-Ashby model was proposed to reveal the relationship between crack length and opening size, applied stress and fracture toughness (Sammis and Ashby 1986). Dzik and Lajtai (1996) further analyzed the influence of opening radius on propagation speed of the primary tensile cracks, and stated that the cracks develop unstably when the radius is greater than 40 mm. To obtain the initiation stresses of the three kinds of fractures, Carter (1991) attached considerable strain gangues to the location of interest around the opening. In fact, it is difficult to arrange the strain gauges because the crack nucleation regions are not clear prior to the loading.

---

[*]Corresponding author, Professor
E-mail: dan.ma@cumt.edu.cn
[a]Ph.D.

ISSN: 2005-307X (Print), 2092-6219 (Online)

Further on, Aker *et al*. (2014), Wang *et al*. (2013), Tao *et al*. (2017), Mellor and Hawkes (1971) and Haeri *et al*. (2015) also explored the failure responses of the circular opening subjected to triaxial loading, dynamic loading, dynamic-static loading and splitting-tensile loading. It is concluded that the loading method is the prominent factor affecting the crack type and sequence. Additionally, rock heterogeneity and discontinuity, ambient temperature and opening filling condition also have been proved to have certain effects on fracture characteristics of openings (Cao *et al*. 2019, Zakharov and Kurilko 2014, Tasdemir *et al*. 1990, Janeiro and Einstein 2010), and the coupling effects will be considered in future work.

Since most of the tunnel sections in rock engineering are horseshoe-shaped and rectangular, it is exceedingly necessary to study the failure behaviors of rock specimens with non-circular openings under loads. For this purpose, Zhu *et al*. (2005) and Zeng *et al*. (2018) numerically and experimentally investigated the impact of opening shape on the mechanical properties and failure mechanism of pre-holed specimens in uniaxial and biaxial compression. The results suggest that the strength and crack evolution are highly dependent on the opening shape. Through the complex variable approach, Wu *et al*. (2020) analytically formulated the initiation stresses and lengths of the primary fractures around different shaped openings under varied stress conditions, which shows good consistency with the experimental results. Weng *et al.* (2018) conducted a number of static-dynamic impact tests on cuboid granite specimens having a square opening with different dip angles via split Hopkinson pressure bar system. Hence made a conclusion that the primary crack speed is reduced as the exerted static stress increases. Additionally, they also argued that the dynamic crack initiation stress and failure modes are associated with the prestress level. With the development of experimental testing methods and equipment, more and more advanced techniques have been developed and used to monitor the cracking growth process, such as: acoustic emission (AE) (Fakhimi *et al.* 2002), nuclear magnetic resonance (Westphal *et al.* 2005), scanning electron microscope (Fonseka, *et al.* 1985), computed tomography (Wennberg and Rennan 2009), electromagnetic radiation (Cress *et al.* 1987) and digital image correlation (DIC) (Maruvanchery and Kim 2020). Accordingly, the initiation, propagation and coalescence behaviors of cracks can be clearly displayed visually and audibly at present. This makes it possible to experimentally examine the failure process of underground openings under stresses.

Given that rock engineering is an aggregation of multiple excavated openings, it addresses a need to investigate the failure mechanisms of rock specimens with two or more openings under loads. However, to date limited literature can be retrieved in this field, and most of the attempts concentrate on the cracking behaviors of circular and square openings in specimens (Tang *et al.* 2005, Huang *et al.* 2019, Jespersen 2010 and Wu *et al.* 2020). Thus, more detailed information regarding the cracking process of specimens containing different numbers of noncircular openings should be investigated further. In our previous research, we reported the crack development around a horseshoe-shaped opening in sandstone rocks in uniaxial compression (Wu *et al.* 2019). On this basis, the AE and DIC equipment was combinedly utilized to deeply study the fracture process of specimens with different quantities of horseshoe-shaped openings under uniaxial loading in this work. Moreover, the failure mechanisms of the specimens were clarified in detail based on the stress distributions. This provides a certain reference for understanding the failure and support design of deep hard rock horseshoe-shaped tunnel group.

2. Experimental materials and methods

2.1 Specimen preparation

Due to the wide distribution and good continuity of sandstone in rock strata, brittle red sandstone stemmed from Linyi of China was selected as the experimental material in this research. Results of the mineralogical tests indicate that the main mineral components of this kind of rock are quartz (0.1~0.3 mm), plagioclase (0.08 × 0.15~0.1 × 0.25 mm), calcite (0.04~0.2 mm), zeolite (0.08 × 0.15~0.1 × 0.2 mm) and K-feldspar (0.05 × 0.1~0.08 × 0.2 mm), as can be seen in Fig. 1 (Luo 2020). According to the suggested methods of the International Society for Rock Mechanics and Rock Engineering (Ulusay and Hudson 2017), we measured the basic physical-mechanical parameters of the fine-grained red sandstone, as given in Table 1.

Considering the possible configurations of tunnel (roadway) system in metal mines, we processed five groups of prismatic specimens in the current study, which were named G1, G2, G3, G4 and G5 in turn, as illustrated in

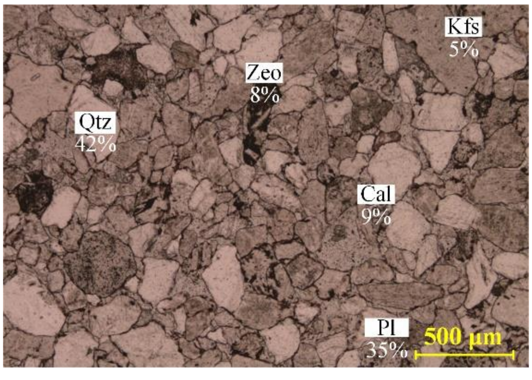

Fig. 1 Micrograph of red sandstone under plane-polarized light (Cal–calcite; Kfs–K-feldspar; Pl– plagioclase; Qtz–quartz; Zeo–zeolite)

Table 1 Physical-mechanical parameters of red sandstone

Density (kg/m^3)	2472.2	Poisson's ratio	0.26
P-wave velocity (m/s)	3174.5	Cohesion (MPa)	19.0
Uniaxial compressive strength (MPa)	99.3	Friction angle (°)	40.4
Tensile strength (MPa)	5.3	Fracture toughness (MPa·m^{½})	0.6
Young's modulus (GPa)	24.4		

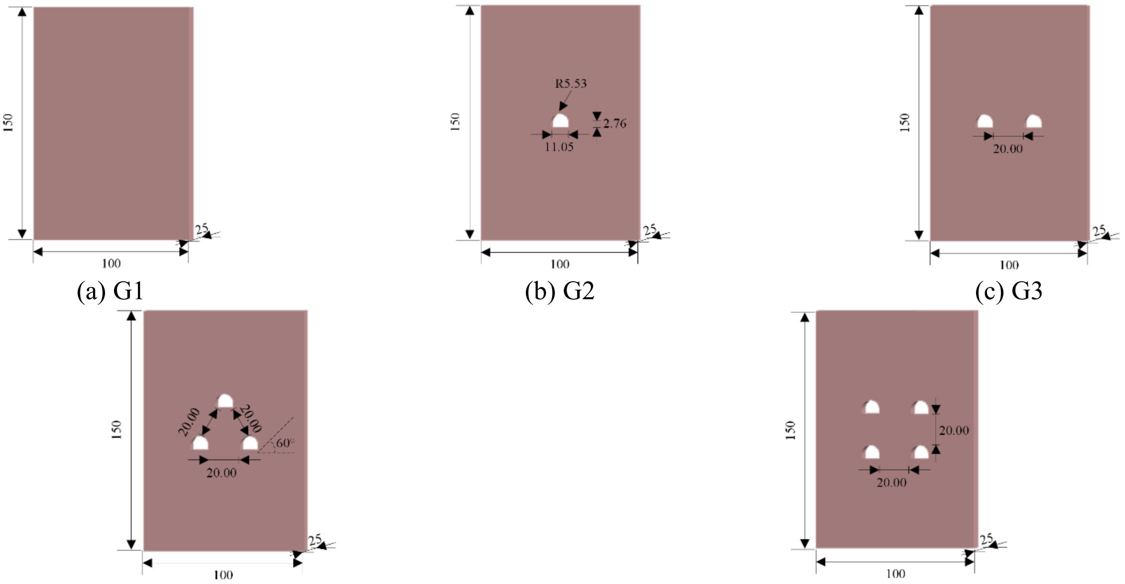

(a) G1 (b) G2 (c) G3

(d) G4 (e) G5

Fig. 2 Schematic diagram of prepared rock specimens (unit: mm)

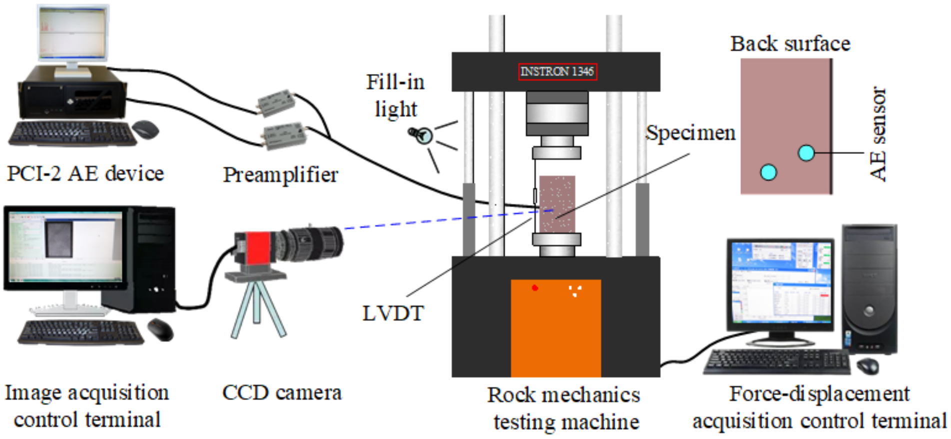

Fig. 3 Experimental facilities

Fig. 2. Each group consists of three identical specimens, and the outline dimensions of the specimens are 100, 25 and 150 mm in width, thickness and height, respectively. The reason why the sample size is designed in this way is mainly based on previous literature (Lee *et al.* 2011, Wu *et al.* 2019). G1 represents the complete specimens, while G2 to G5 denote the specimens containing one to four horseshoe-shaped openings, respectively. Note that the inverted U shape is exactly the same as the tunnel section shape commonly used in rock engineering. The prefabricated openings in the specimens were precisely excavated by high-pressure water jet technology, and each opening possesses the same cross-sectional area. For the specimens having two or more openings, the spacing between the two adjacent openings is 20 mm. The reason why the spacing size is so designed is that it is greater than three times the tunnel radius, and it is basically in line with the layout of the tunnel system in mining engineering, such as the sublevel haulage (drill) roadways in sublevel stoping mining method or across-vein roadways in pillarless sublevel caving method.

2.2 Experimental facilities

All the uniaxial compression tests on the specimens were performed at the Advanced Research Center of Central South University in China. The main experimental facilities used are: rock mechanics testing machine, AE device and DIC instrument, which is presented in Fig. 3.

Instron 1346 is a multi-purpose tester that can measure the mechanical parameters of tension, compression, shearing and bending of rock materials. The maximum load of the apparatus reaches 2000 kN, and the measurement accuracy is up to ±0.5%. During the tests, to ensure that the right amount of images is collected, the displacement-controlled loading rate is set to 0.6 mm/min. The real-time load imposed on the specimens can be recorded and stored by the force-displacement acquisition control terminal. Besides, a linear variable differential transformer (LVDT) was installed between the upper and lower loading plates to monitor the continuous deformation of the specimens.

Since the rock will emit sound waves during the fracture process, the damage and fracture characteristics of the

Table 2 Mechanical properties of rock specimens subjected to uniaxial compression

Specimen Number	Length (mm)	Width (mm)	Height (mm)	Density (kg.m^{-3})	σ_p (MPa)	ε_p (‰)	E (GPa)
G1-A	100.1	25.0	150.1	2391.4	100.9	5.57	21.63
G1-B	99.6	24.9	150.5	2427.5	105.6	5.96	21.63
G1-C	100.7	24.8	150.7	2385.5	101.3	6.97	19.07
G2-A	100.4	25.5	150.3	2462.2	89.22	6.08	16.90
G2-B	100.8	24.7	151.0	2415.4	78.50	6.01	14.95
G2-C	100.8	24.9	151.1	2404.6	77.95	6.23	14.95
G3-A	100.0	25.0	149.5	2328.2	58.34	4.61	16.10
G3-B	100.0	25.1	150.3	2350.7	56.21	3.79	15.98
G3-C	99.6	25.4	150.3	2367.3	59.34	3.82	16.55
G4-A	99.6	25.8	150.7	2365.0	75.84	5.19	17.46
G4-B	99.5	24.8	150.3	2332.2	71.35	4.52	17.05
G4-C	99.7	25.0	150.8	2318.1	68.03	4.50	17.86
G5-A	100.0	25.0	149.5	2328.2	58.34	4.61	16.10
G5-B	100.0	25.1	150.3	2350.7	56.21	3.79	15.98
G5-C	99.6	25.4	150.3	2367.3	59.34	3.82	16.55

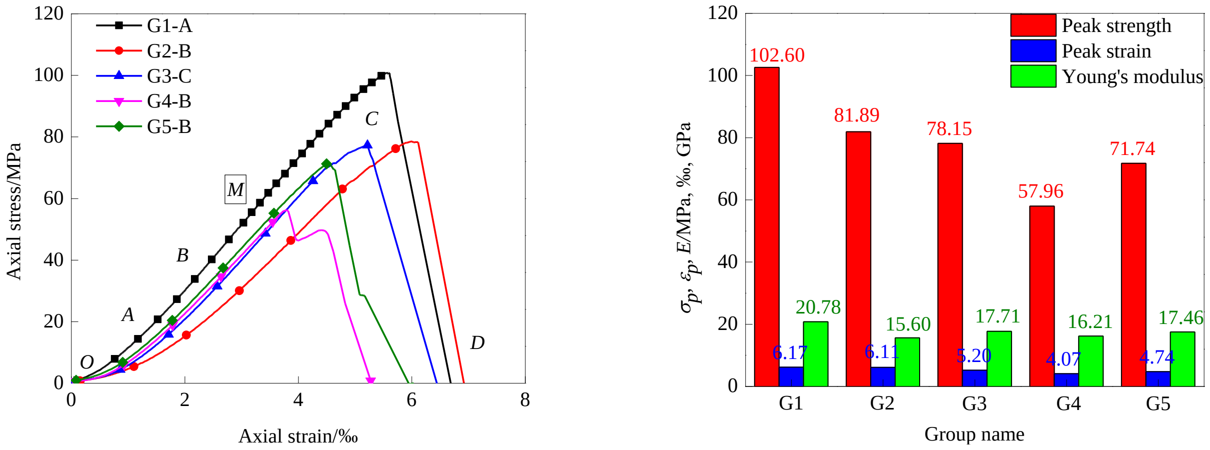

(a) Stress-strain curves (b) Mechanical property parameters

Fig. 4 Experimental results of specimens under uniaxial loading

sample can be evaluated based on the sound wave signals. In this study, a set of AE system from Physical Acoustics Co. was adopted to monitor the AE count. This system comprises one PCI-2 AE device, two 2/4/6 preamplifiers with a gain of 40 dB as well as two pico-type AE sensors attached to the back surface of the specimen. To reduce the interference of environmental noise, the detection threshold of the AE device is set to 45 dB. The signal acquisition frequency is determined as 10 Msps, and the AE Win software was applied for data recording and signal processing. Also, the acquisition parameters of the AE system such as the sampling rate, peak definition time (PDT), hit definition time (HDT) and hit lockout time (HLT) were set at 10 Msps, 50 μs, 20 μs and 300 μs, respectively.

As an effective tool to measure the full-field deformation of rock specimens, DIC technique is widely used to monitor the crack development in the field of rock mechanics (Yamaguchi 1981, Choi and Shah 1997). Its basic principle is: based on image recognition technology, the positions of points on the specimen surface before and after deformation can be tracked, and then the displacement and strain can be calculated by digital image processing. To exactly identify the positions of the points on the image, white paint and black paint were sprayed successively on the specimen surface to form a thin layer of randomly distributed speckles during the specimen preparation. More detailed description concerning the speckle production and reliability verification of this technique is presented in reference (Wu *et al.* 2019). Generally, DIC system is composed of one CCD camera, one fill-in light and one image acquisition control terminal. The selected CCD camera made by Basler Vision Technology owns a maximum photo acquisition speed of 17 frames/s (2456 × 2058 pixels in resolution), and it was installed 1.0 m directly in front of the speckle surface of the specimen. In the image acquisition control terminal, we set the size and acquisition frequency of the image to 1100 (width) × 1500 (length) pixels and 15 FPS. Also, a fill-in light was placed

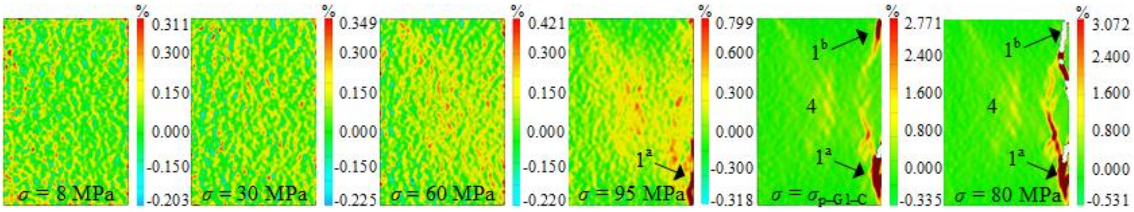

(a) Specimen G1-C

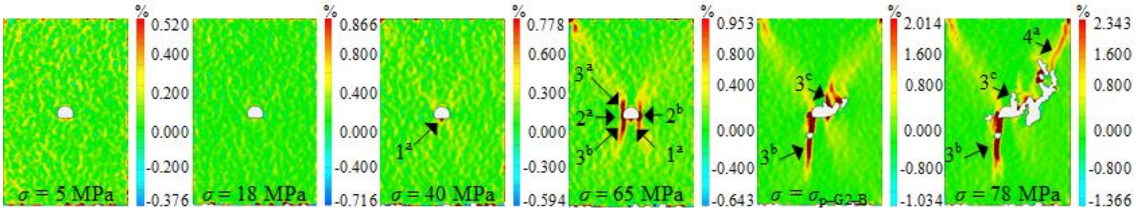

(b) Specimen G2-B

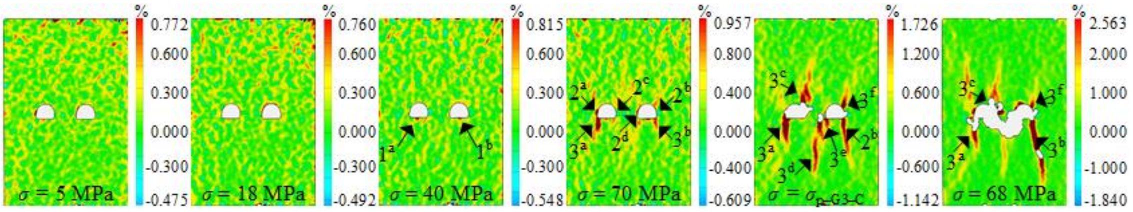

(c) Specimen G3-C

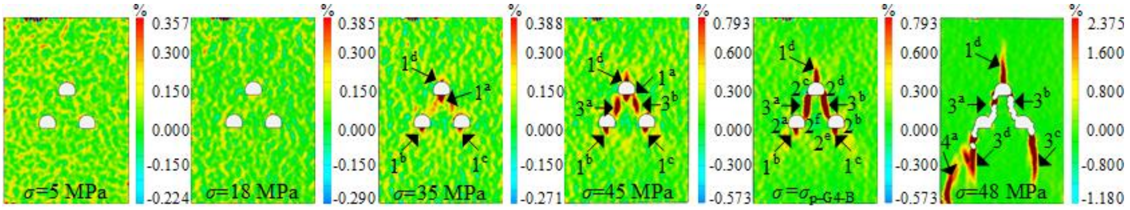

(d) Specimen G4-B

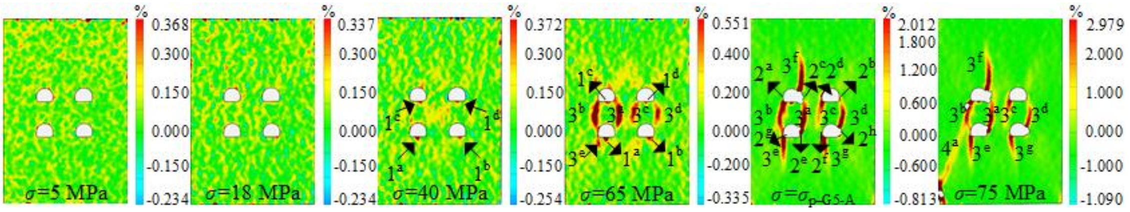

(e) Specimen G5-A

Fig. 5 Maximum principal strain distributions of specimens during uniaxial compression tests

near the specimen to improve the clarity of the photos. Based on the recorded photos of the specimen at different deformation moments, the strain field and displacement field of the specimen can be generated using GOM Correlate software. To ensure that all monitoring parameters correspond to the loading time, the above experimental apparatus are required to start concurrently.

3. Experimental results and analysis

3.1 Axial stress-strain curves

Based on the recorded experimental data, we can plot the axial stress-strain curves of the specimens and obtain the mechanical property parameters (see Table 2). Fig. 4(a) illustrates the tested curves of five representative specimens under uniaxial loading. It can be observed that all the curves present a typical ′S′ shape before the peak point, and drop sharply at the end of the experiments. Obviously, the brittleness of the specimens is extremely remarkable. According to the change characteristics of the curves, we can divide the deformation process into four stages, namely: the micro-defect compaction stage (OA), elastic deformation stage (AB), cracking stage (BC) and post-peak instability stage (CD). Based on the crack evolution law, the cracking stage can be further divided into two substages: stable fracture (BM) and unstable fracture (MC), which is described in detail in the next section. Additionally, it is also observed that the stress-strain curves of the specimens having openings fluctuates near the peak, which is caused by the sudden appearance or coalescence of cracks.

Fig. 4(b) shows the average values of uniaxial compressive strength (σ_p), peak strain (ε_p) and Young′s modulus (E) of the five groups of specimens. The average strength value of group G1 is 102.60 MPa, while that of groups G2 to G5 is 81.89, 78.15, 57.96 and 71.74 MPa, respectively. This suggests that the strength of the rocks is appreciably reduced by the openings. Compared with the intact specimens, the strength reduction rate of groups G2 to G5 is 20.19%, 23.83%, 43.51% and 30.08%, respectively. Likewise, the peak strain and Young′s modulus of the specimens containing openings are also decreased to different degrees in comparison with those of the intact specimens. Generally speaking, the larger the number of openings, the worse the bearing capacity of the specimen. Interestingly, the group G5 exhibits higher strength and stiffness than the group G4, which can be explained by the internal stress distributions of the specimens (see Section 4).

3.2 Cracking behavior and failure phenomenon

By importing the collected photos of the specimens to the GOM Correlate software for processing, the full-field strains and displacements of the specimens subjected to uniaxial compression can be visually reproduced. According to the change of the maximum principal strain field, the evolution of the cracks represented by strain localization can be clearly shown. To fully understand the failure processes of the specimens with a different number of openings under uniaxial loading, we selected five representative specimens to describe the cracking behavior. For each specimen, a total of six maximum principal strain nephograms representing different deformation moments during the loading process were picked out, and these moments correspond to the various deformation stages in Fig. 4(a), as shown in Fig. 5. The meanings of the notes in the subfigures are defined as follows: the number represents the type of crack, where 1, 2, 3 and 4 denote the first-tensile cracks, spalling cracks, second-tensile cracks and shear cracks, respectively; the lowercase letters superscripted on the number mean the order in which the cracks appear.

Fig. 5(a) illustrates the variation of the maximum principal strain distribution inside the intact specimen during uniaxial compression. It can be observed that when the axial stress is 8 MPa, some randomly distributed yellow dots appear, which means that the protogenous micro-defects such as pores and cracks inside the specimen are closed under compression. When the stress increases to 30 MPa, the number of yellow dots in the specimen is basically unchanged due to the elastic deformation. With the gradual increase of the stress, the number of yellow dots increases, and some of them become red high strain points. At a stress of 95 MPa, one first-tensile crack 1^a emerges in the lower right corner of the specimen and grows along the loading direction. At the peak stress, the other first-tensile crack 1^b occurs in the upper right corner of the specimen. After the peak, the two cracks are gradually connected, and a yellow shear band appears on the diagonal of the specimen and finally grows into a shear crack 4. This contributes to shear-type failure mode.

For specimen containing one single horseshoe-shaped opening, the maximum principal strain distributions in the first two deformation stages are similar to those of the intact rock specimen, which can be seen in Fig. 5(b). When stage BM is approached, one first-tensile crack 1^a occurs at the floor of the opening. Since it propagates downwards and stably, this period of deformation is also called the stable fracture stage. After that, the sample enters the unstable fracture stage (MC). In this stage, spalling cracks 2^a and 2^b appear on both sides of the opening, causing the nearby rock to flake off and the formation of V-shaped failure zones (Lee *et al*. 2020b). Meanwhile, several sub-vertical second-tensile cracks are found to emerge on the corners of the opening and develop rapidly towards the V-shaped failure zones. At the peak stress, two main second-tensile cracks 3^b and 3^c have been penetrated with this opening. Yellow bands were observed on the diagonals of the specimen, and they will eventually evolve into shear cracks. Lastly, the specimen fails due to the coalescence of the shear cracks and V-shaped failure zones of the openings. Compared to the research results of our previous work, we found that no first-tensile crack occurs on the roof of the opening. This may result from the small size of the opening (Peng *et al*. 2015, Lotidis *et al*. 2019).

As shown in Fig. 5(c), the crack evolution of the specimen with two horseshoe-shaped openings during the test can also be clearly presented according to the development of strain localization. In the first two deformation stages, the maximum principal strain distribution characteristics are similar to those of the above two specimens. At the stable fracture stage, two first-tensile cracks 1^a and 1^b are generated at the bottom of the two openings almost simultaneously. Next, the spalling cracks 2^a~2^d occur on the sidewalls of the two openings. When the stress continues to increase to the peak, a few second-tensile cracks 3^a~3^f are formed on the corners of the two openings and grows straightly towards the spalling zones. As the V-shaped failure zones are getting larger and larger, the two openings are connected in the post-peak stage. At last, one shear crack in the lower left corner of the specimen extends to the left opening and the second-tensile crack 3^c propagates to the upper end, leading to shear-tensile failure mode. Due to the significant brittleness of the rock, the post-peak period is very short, leading to difficulties in collecting enough photos to characterize the post-peak fracture behavior.

With regard to the specimen having three horseshoe-shaped openings, the failure process can also be reproduced by the DIC technique. As illustrated in Fig. 5(d), with the rising stress from 5 MPa to 18 MPa, there are no macro cracks except some yellow spots. When reaching the stable fracture stage, the first-tensile cracks 1^a~1^c are found at the bottom of the three openings. Moreover, it is observed that another first-tensile cracks 1^d is formed on the top of the upper opening. This is because the tensile stress in this area is relatively large. At a stress of 45 MPa, two second-tensile cracks 3^a and 3^b appear between the upper and lower openings. When the stress increases to the peak value, spalling failure is found to occur on the sides of these openings, and the top and bottom openings are nearly linked by the second-tensile cracks 3^a and 3^b. When the axial stress approaches 48 MPa at the post-peak stage, we can see that two other second-tensile cracks 3^c and 3^d are formed in the lower-left corner of the lower-left opening and the lower-right corner of the lower-right opening. At the same time, it is observed that the upper and lower opening have got coalesced. Besides, one shear crack 4^a occurs and

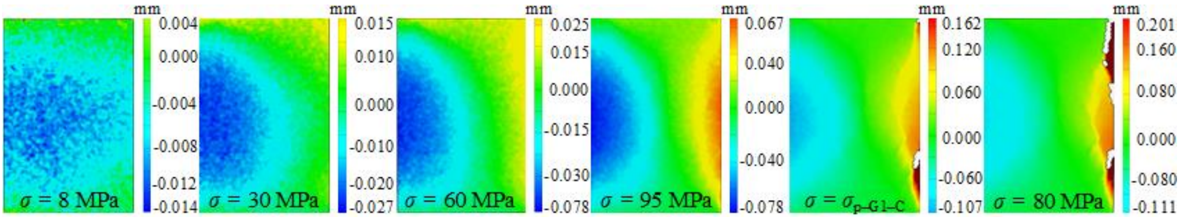

(a) Specimen G1-C

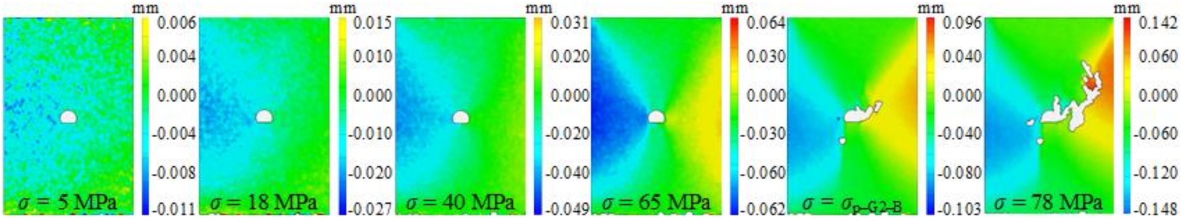

(b) Specimen G2-B

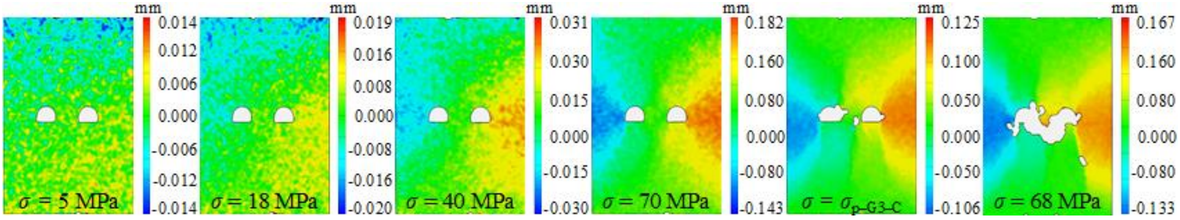

(c) Specimen G3-C

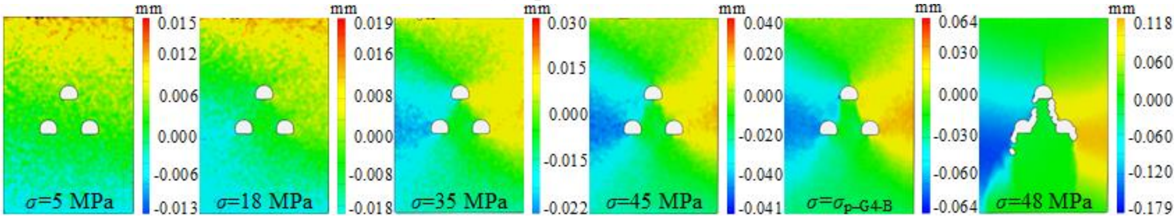

(d) Specimen G4-B

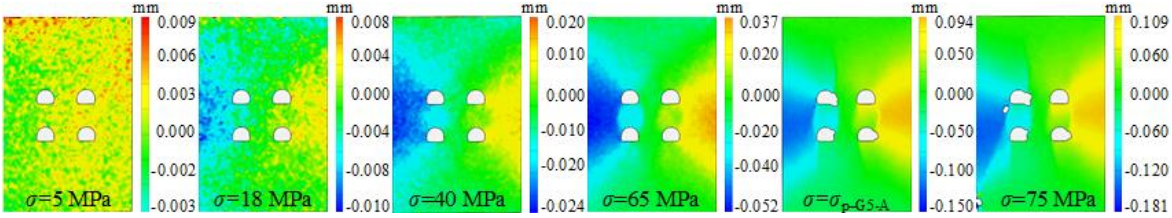

(e) Specimen G5-A

Fig. 6 Horizontal displacement distributions of specimens during uniaxial compression tests

propagates along the diagonal. Finally, the shear cracks extend to the lower openings and the second-tensile crack 1^d propagate to the upper end of the specimen, resulting in a shear-tensile failure mode.

The maximum principal strain distributions of the specimen with four horseshoe-shaped openings at different loading times are given in Fig. 5(e). From the figure, the crack development including crack initiation, propagation and coalescence can be clearly demonstrated. When the applied stress is small, i.e., in the first two deformation stages, no macroscopical cracks are found to occur. At axial stress 40 MPa, one first-tensile crack appears at the bottom of each of the four openings. Afterwards, four second-tensile cracks 3^a~3^d are formed between the upper openings and the lower openings. When the applied stress approaches the peak, spalling failure happens on both sides of the openings. This brings about the formation of V notches. Further on, three other second-tensile cracks emerge around the openings. When the post-peak stress is reduced to 75 MPa, a shear crack is found to initiate from the lower left corner of the specimen and extends toward the opening. At last, the failure of the specimen is induced by the connection of the shear crack 4^a and the second-tensile cracks 3^b and 3^f, which can be classified as shear-tensile failure mode.

Besides, it is further observed that the first-tensile cracks close gradually as the second-tensile cracks develop. When the lateral extrusion is released, namely the experiment ends, the first-tensile cracks reopen. For the white areas that emerges around the opening in the figures, they are caused by surface spalling of the specimen. From the above, we can conclude that the fracture behaviors of the specimens can be well characterized by the maximum principal strain distribution. By the DIC technology, we can

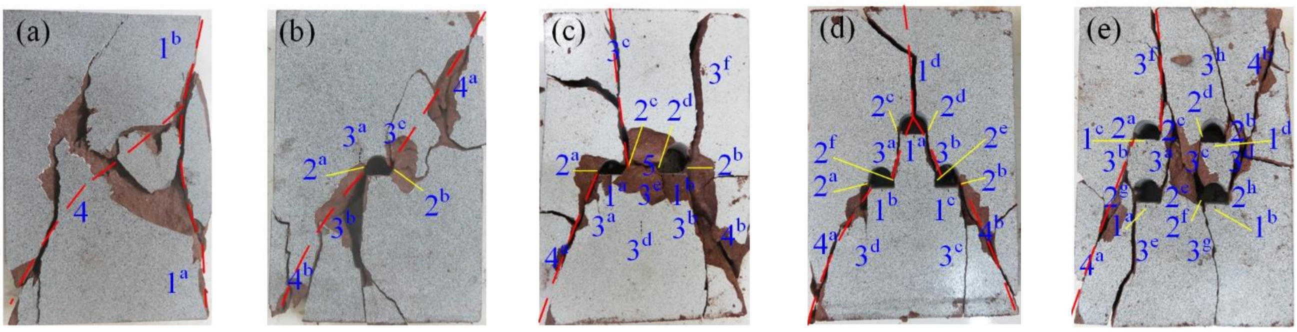

Fig. 7 Failure states of specimens under uniaxial compression: (a) specimen G1-C, (b) specimen G2-B, (c) specimen G3-C; (d) specimen G4-B and (e) specimen G5-A

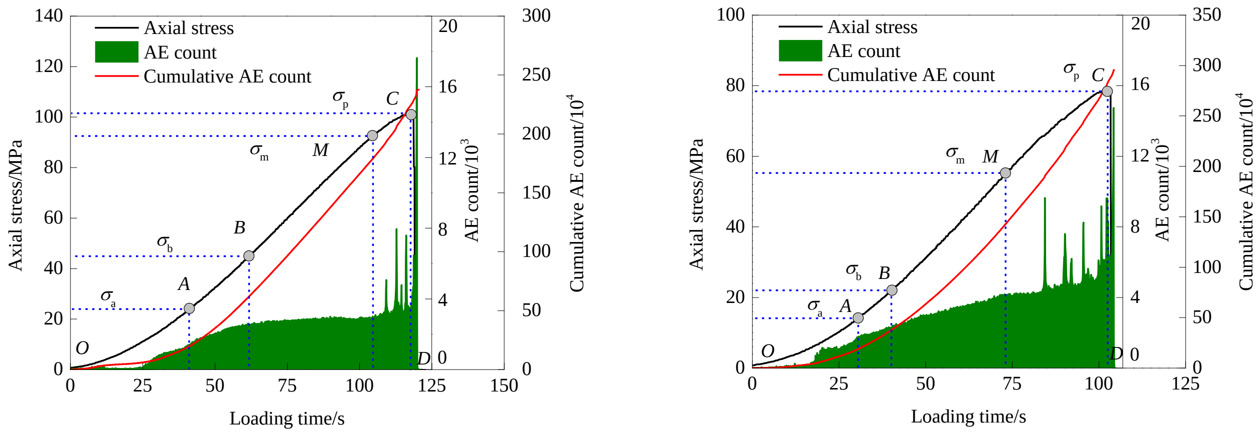

(a) Specimen G1-C

(b) Specimen G2-B

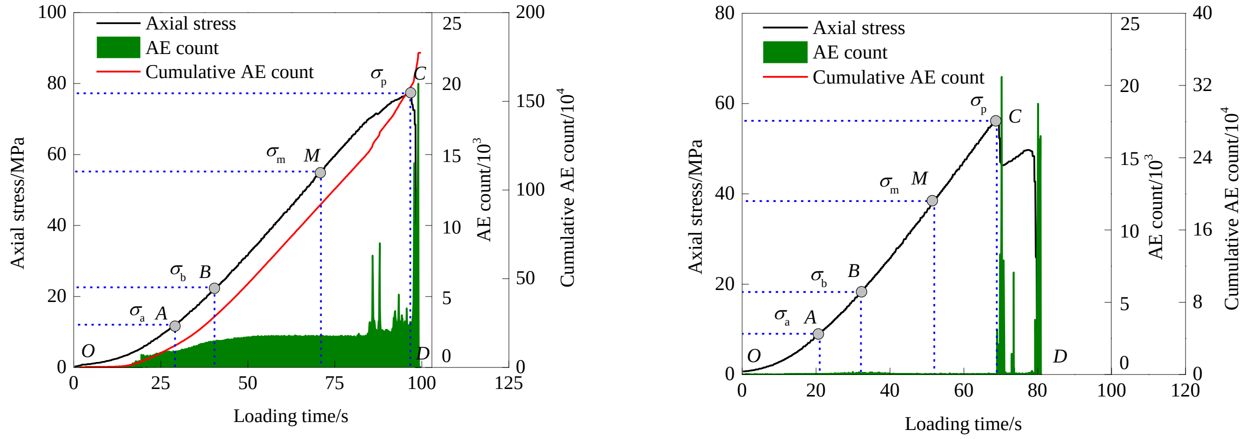

(c) Specimen G3-C

(d) Specimen G4-B

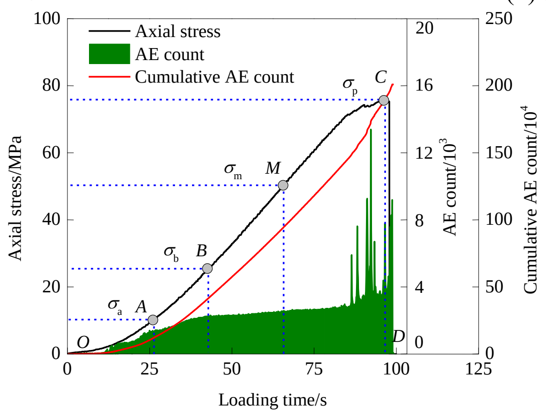

(e) Specimen G5-A

Fig. 8 AE signals of specimens under uniaxial compression also obtain the horizontal displacement distributions of the above specimens under different loading stresses, as presented in Fig. 6.

In Fig. 6, the sign convention of the displacement is as follows: the displacement is positive when the rock particle moves to the right, otherwise it is negative when the rock particle moves to the left. Taking the intact specimen as an example, as the applied stress increases, a blue moon-shaped area with a gradually increasing displacement appears in the left half of the specimen. When the stress rises to 95 MPa, a yellow triangle area symmetrical to the blue area occurs in the right half of the specimen. This suggests that the blue area and the yellow area of rock deform towards the left and the right, respectively. In contrast, the color of the middle part of the specimen is green, indicating the amount of deformation is small. Obviously, cracks are most likely to occur at the boundaries of different color areas. At the peak stress, it is found the triangular area changes from yellow to red, and the boundary lines representing the first-tensile cracks 1^a and 1^b become more and more clear. After the peak, the color of the moon-shaped area completely changes to cyan, and the boundaries located on the diagonals of the specimen are getting clearer. This agrees well with the situation of the shear band in Fig. 5(a). Similarly, the cracking processes of the specimens having openings can be revealed based on the horizontal displacement distribution during the tests. To conclude, the cracking behavior characterized by the horizontal displacement field are basically consistent with that by the maximum principal strain field.

The final failure states of the above specimens under uniaxial compression are illustrated in Fig. 7. In the figure, the red line denotes the failure path. Thus, it is summarized that the failure of the specimen having an opening belongs to the shear-dominated failure mode, while the failure modes of the rest specimens are classified as the mixed tensile-shear failure. It should be noted that since the DIC device can only capture one or two photos of the specimen after the peak, the final damage state looks a bit different from that in the post-peak stage. Also, it is observed that some cracks or surface cracks emerge during the unloading process, which do not play a leading role in the failure mode of the specimen.

3.3 AE signal features and crack threshold stresses

AE refers to the generation of transient elastic waves produced by a sudden release of energy from localized sources. Sources of AE vary from natural and artificial events such as earthquake and rock burst to the initiation and development of cracks in solid materials. Monitoring and evaluation of AE signals can provide useful information concerning the fracture behavior of rock material. Since the ringing count could reflect the amplitude of AE signal to a certain extent, the real-time AE count and cumulative AE count of the above five representative specimens were detected, as illustrated in Fig. 8. Besides, the curves of axial stress versus loading time are also plotted as a reference.

In Fig. 8, we can also divide the AE process into five stages, which matches the deformation stages. In the first stage, the AE activity is not very active because of the closure of the micro-defects under compression. When the elastic stage is approached, the deformation of the specimen can be recovered and only few cracks are formed. As a result, the AE count increases very slowly. At the stable fracture stage, the number of the AE count basically remains unchanged due to the stable propagation of the first-tensile cracks. After that, it is observed that the number of the AE count of the specimen with openings increases gradually. This is attributed to the occurrence of the spalling cracks. When the exerted stress is close to the peak, the number of the AE count grows sharply. Obviously, this is induced by the appearance of the second-tensile cracks and their coalescence with the V-shaped failure zones. At the post-peak stage, the number of the AE count and the cumulative AE count both rise significantly, which is caused by the brittle failure. Overall, it can be seen that the fracture characteristics reflected by AE signals are in fair agreement with that reflected by the maximum principal strain distributions. Additionally, it is proved that the fluctuation of the stress-strain curve before the peak is induced by the sudden appearance of the second-tensile cracks and their penetration with the V-shaped failure zones.

Table 3 Crack threshold stress values of specimens during fracture process

Specimen Number	σ_a/MPa	σ_b/MPa	σ_m/MPa
G1-C	24.2	44.8	92.2
G2-B	14.0	21.2	55.2
G3-C	12.0	22.9	55.1
G4-B	9.0	18.3	38.3
G5-A	10.1	25.4	50.3

As can be seen in Fig. 8, several crack threshold stresses are related during the fracture process, that is, the crack closure stress (σ_a), crack initiation stress (σ_b) and crack damage stress (σ_m). The crack closure stress is the axial stress corresponding to the cut-off point at the micro-defect compaction stage and the elastic deformation stage on the stress-strain curve. In this study, the method proposed in our previous study (Wu *et al.* 2019) was used to determine its value. For the crack initiation stress, it can be obtained by using the DIC and AE techniques. When the AE count increases markedly for the first time and the strain localization is formed in the specimen, indicating that the first-tensile cracks start to grow and the corresponding stress at this time is the crack initiation stress. With regard to the crack damage stress, we can also derive it combining the AE signal change and the maximum principal strain distribution. When the AE count increases significantly for the second time and spalling cracks appear on both sides of the opening, it can be considered that the damage stress has been reached. Table 3 shows the crack threshold stress values of the representative specimens subjected to uniaxial loading. It is found that the crack threshold stress values of the specimens having openings are lower than those of the intact specimen. The crack closure stresses of the specimens containing holes are basically equal. For the crack initiation stress, the value of the specimen G4-B is the smallest

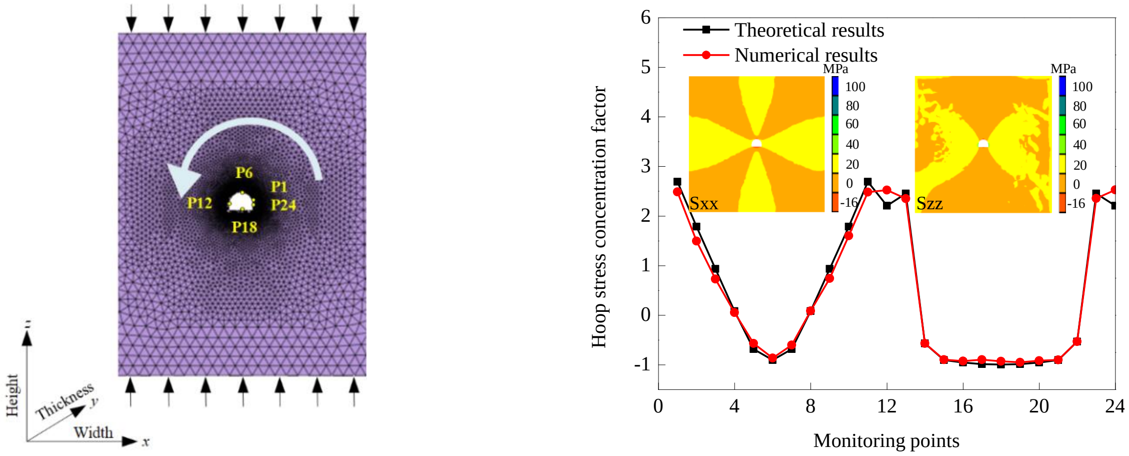

(a) Layout of monitoring points in model G2 (b) Theoretical and numerical results of model G2

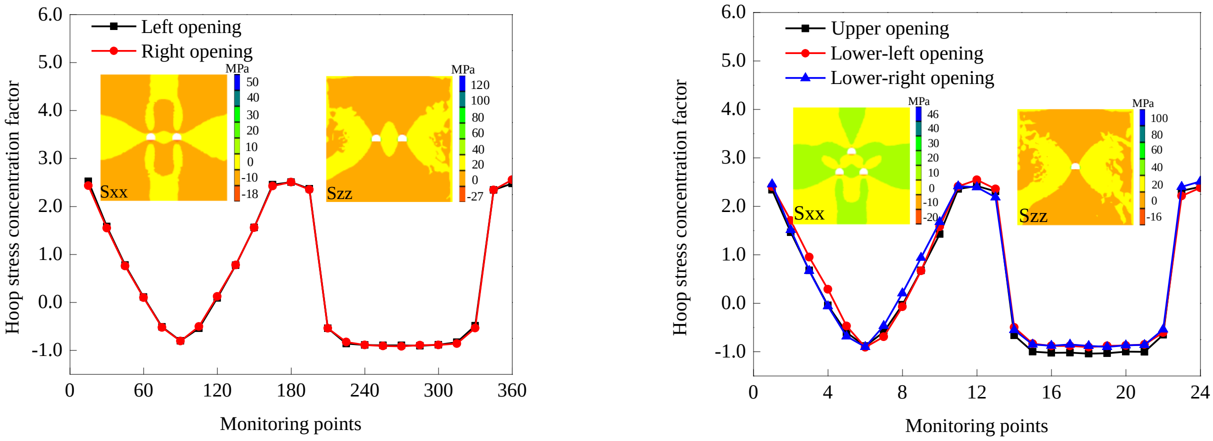

(c) Numerical results of model G3 (d) Numerical results of model G4

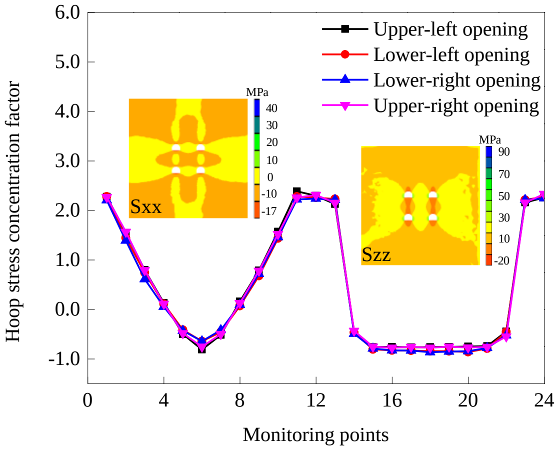

(e) Numerical results of model G5

Fig. 9 Hoop stress concentration factor on the perimeter of openings in rock models under uniaxial compression

among the specimens containing openings, while that of the specimen G5-A is the largest. With respect to the crack damage stress, the value of the specimen G4-B is also the smallest, while that of the specimen G2-B is the largest. These are consistent with the strength of the specimens and the order of crack initiation.

4. Discussion on fracture mechanism

As stated in Section 3, the fracture process of the specimens with pre-existing openings under uniaxial compression develops from first-tensile cracks (spalling cracks), then second-tensile cracks that become shear cracks. The difference lies in the number of initiated cracks and cracking sequence as well as the failure mode, which mainly depends on the opening number. In fact, the initiation and growth of cracks are triggered by the stress. Therefore, it is essential to realize the stress states around the openings in specimens under uniaxial loads.

In this work, FLAC code (ITASCA Consulting Group) was used to simulate the stress distributions around the openings. Considering the boundary effect, the size of the model should be sufficiently larger than that of the openings. The selected width, thickness and height of the rock models were therefore 100.0, 25 and 150.0 mm, respectively. The dimensions of the openings and the models are the same as those of the rock sample above. A total of four models containing one to four horseshoe-shaped openings were constructed, namely models G2, G3, G4 and G5. As the specimen is in an elastic state before the crack initiates. Thus, clarifying the internal stress distribution of the specimen in the elastic stage is of great significance to reveal the fracture mechanism. To avoid the occurrence of plastic deformation caused by opening excavation, the values of shear modulus and bulk modulus are both set large. The model grid was automatically divided, i.e., the grid size of the zones close to the openings was 0.1 mm, while that away from them was 5.0 m. A constant stress of 20 MPa was applied to the upper and lower ends of the models, and the elastic constitutive model was adopted for modelling. Obviously, the states of the specimens under such a stress are at elastic stage. To grasp the distribution law of stress around the openings, 24 monitoring points named from P1 to P24 are evenly arranged in the counterclockwise direction on the perimeter of each opening. Through program execution, the horizontal and vertical stresses (Sxx and Syy) of all monitoring points can be directly obtained, and then the hoop stress concentration factor (SCF) can be calculated, as shown in Fig. 9.

Taking the case of the model having one single opening as an example, it is found that the tensile stress concentration occurs on the top and bottom of the opening, and the maximum values of the SCFs are -0.87 and -0.93 respectively. By comparison, the two sides are concentrated by high compressive stresses, with a maximum SCF of 2.52. According to our previous work, for single openings with simple shape, the stress states can be analytically derived using complex variable method (Wu *et al.* 2020). The comparison of the theoretical and simulation results is shown in Fig. 9b, which suggests that the numerical method is reliable. Actually, the slight difference is caused by the large size of the grids (Wu *et al*. 2021, Dang *et al*. 2019). Therefore, the first-tensile cracks are formed at the roof and floor of the opening when the tensile stress is larger than the tensile strength, while the spalling cracks emerge at the two sides if the concentrated compressive stress exceeds the shear strength or cohesion of the specimen. As a result, the V-shaped failure zones occur. As the first-tensile cracks propagate away from the cavity, the critical stress region shifts from the tips of the first-tensile cracks to a region on either side of the first-tensile cracks. That is to say, the first-tensile cracks stop growing when they reach a certain length, and the second-tensile cracks begin to develop from the corners of the opening towards the sidewalls. At last, the second-tensile cracks will connect the V-shaped failure zones. For the shear cracks on the diagonal, they are induced by the shear stress formed by the resultant force of the applied load and the horizontal friction at the end of the specimen. Once the resultant force is larger than the shear strength, the shear cracks start to appear.

Similarly, the stress distributions in specimens containing two to four openings under 20 MPa in the vertical direction can also be numerically obtained, as presented in Figs. 9(c) to 9(d). The law of stress distribution is similar, that is, tensile stress areas are formed at the top and bottom of the openings, and compressive stress concentrated areas appear on both side walls. In regard to the rock model with two openings, the maximum SCFs in the roof and floor of the openings are -0.81 and -0.91, respectively. Moreover, the maximum SCFs on the left side wall of the left opening and the right side wall of the right opening are both 2.53, and those on the right side wall of the left opening and the left side wall of the right opening are both equal to 2.49. This is caused by the superposition of the compressive stress concentration in the rock bridge area between the openings. Likewise, we can plot the SCFs of all the monitoring points around the three and the four openings. The slight difference in stress distribution is the stress level. For the model with three openings, the maximum SCFs in the top and bottom locations of the upper opening are -0.89 and -1.04, respectively, and those of the lower two openings are -0.91 and -0.90, respectively. For the maximum SCFs on the sides of the three openings, the values are both 2.41 for the upper opening, while those of the lower two openings are 2.53 and 2.39. It can be seen that the compressive stress concentration degree of the rock bridge in the specimen having three openings is weaker than that in the specimen having two openings. This results from the influence of tensile stress area of the upper opening. In terms of the stress distribution in the specimen having four openings, the maximum SCFs in the roofs and floors of the upper two openings are -0.78 and -0.77, respectively; while those of the lower two openings are -0.65 and -0.85, respectively. With respect to the maximum SCFs on the sides of the openings, the values of the upper two openings are 2.32 and 2.19, while those of the lower two openings are 2.26 and 2.25. By comparing the stress distribution around the three-openings and four-openings, it is concluded that the four-openings have a weaker stress concentration and therefore have relatively high strength. The larger the maximum tensile stress, the smaller the crack initiation stress. In summary, the stress distribution around the openings can explain the type and sequence of cracks well. Also, it is proved that there are good correlations between the order of the maximum tensile SCF in the roof and floor of the four types of pre-holed models and the order of the crack initiation stress of the four kinds of the specimens with openings.

Besides, the in-situ stress states of underground tunnels in rock mass are two or three dimensional, thus conducting biaxial and triaxial compression tests on the rock specimens having openings is quite necessary and significant for engineering practice. This is also the limitation of this work, but the useful finding is still important for the understanding of tunnel instability in the case where the principal stress of the tunnel is the vertical stress. As the mechanical properties and fracture mechanism of specimens having multiple non-circular openings are still not fully understood, we continue to focus on the uniaxial loading method in this study. However, further experimental or numerical study will be performed on these specimens under biaxial and triaxial compression in the near future.

5. Conclusions

In this study, the fracture response and mechanisms of brittle rock failure with a different number of openings under uniaxial compression were examined. From the experimental and numerical results, several conclusions can be drawn as follows.

- The pre-existing presence of horseshoe-shaped openings significantly reduces the uniaxial compressive strength, peak strain and Young′s modulus of the rock specimens, and the size of reduction depends largely on the number of the openings. However, the mechanical performance of the specimens having four openings are larger than those of the specimens having three openings.
- Fracture characteristics of the specimens having openings under uniaxial loading can be efficiently presented based on the changes of the maximum principal strain and the AE signal. A total of four patterns of cracks around the openings are observed, that is, first-tensile cracks, second-tensile cracks, spalling cracks and shear cracks. Several crack threshold stresses during the fracture process can be measured combining DIC and AE techniques. For the failure modes, the single-opening specimens are shear dominant, while the other types of specimens are tensile-shear mixed.
- According to the internal stress distribution law of the specimen under axial load, the crack evolution mechanism is clearly identified, namely the first-tensile cracks are caused by the tensile stress concentration on the roof and floor of the opening, the spalling cracks results from the concentrated high compressive stresses on the sides of the opening, the second-tensile cracks are induced by the tensile stress on the corners of the opening, and the shear cracks are triggered by the shear stress on the diagonal of the specimen.

Acknowledgments

This research was supported by the Fundamental Research Funds for the Central Universities (2021QN1010).

References

Aker, E., Kühn, D., Vavryčuk, V., Soldal, M. and Oye, V. (2014), “Experimental investigation of acoustic emissions and their moment tensors in rock during failure”, *Int. J. Rock Mech. Min. Sci.*, **70**, 286-295. https://doi.org/10.1016/j.ijrmms.2014.05.003.

Cao, R.H., Cao, P., Lin, H., Fan, X., Zhang, C.Y. and Liu, T.Y. (2019), “Crack Initiation, propagation, and failure characteristics of jointed rock or rock-like specimens: A review”, *Adv. Civ. Eng.*, 6975751. https://doi.org/10.1155/2019/6975751.

Carter, B.J., Lajtai, E.Z. and Petukhov, A. (1991), “Primary and remote fracture around underground cavities”, *Int. J. Numer. Anal. Met.*, **15**(1), 21-40. https://doi.org/10.1002/nag.1610150103.

Choi, S. and Shah, S.P. (1997), “Measurement of deformations on concrete subjected to compression using image correlation”, *Exp. Mech.*, **37**(3), 307-313. https://doi.org/10.1007/BF02317423.

Cress, G.O., Brady, B.T. and Rowell, G.A. (1987), “Sources of electromagnetic radiation from fracture of rock samples in the laboratory”, *Geophys. Res. Lett.*, **14**(4), 331-334. https://doi.org/10.1029/GL014i004p00331.

Dang, W.G., Konietzky, H., Herbst, M. and Frühwirt T. (2020), “Cyclic frictional responses of planar joints under cyclic normal load conditions: Laboratory tests and numerical simulations”, *Rock Mech. Rock Eng.*, **53**, 337-364. https://doi.org/10.1007/s00603-019-01910-9.

Dang, W.G., Wu, W., Konietzky, H. and Qian, J.Y. (2019), “Effect of shear-induced aperture evolution on fluid flow in rock fractures”, *Comput. Geotech.*, **114**, 103152. https://doi.org/10.1016/j.compgeo.2019.103152.

Dzik, E.J. and Lajtai, E.Z. (1996), “Primary fracture propagation from circular cavities loaded in compression”, *Int. J. Fract.*, **79**(1), 49-64. https://doi.org/10.1007/BF00017712.

Fakhimi, A., Carvalho, F., Ishida, T. and Labuz, J.F. (2002), “Simulation of failure around a circular opening in rock”, *Int. J. Rock Mech. Min. Sci.*, **39**, 507-515. https://doi.org/10.1016/S1365-1609(02)00041-2.

Fonseka, G.M., Murrell, S.A.F. and Barnes, P. (1985), “Scanning electron microscope and acoustic emission studies of crack development in rocks”, *Int. J. Rock Mech. Min. Sci.*, **22**(5), 273-289. https://doi.org/10.1016/0148-9062(85)92060-1.

Haeri, H., Khaloo, A. and Marji, M.F. (2015), “Fracture analyses of different pre-holed concrete specimens under compression”, *Acta Mechanica Sinica*, **31**(6), 855-870. https://doi.org/10.1007/s10409-015-0436-3.

Hoek, E. (1965), “Rock fracture under static stress conditions”, Research Report No. MEG383, University of Cape Town, Pretoria, The Republic of South Africa.

Huang, Y.H., Yang S.Q. and Tian, W.L. (2019), “Cracking process of a granite specimen that contains multiple pre-existing holes under uniaxial compression”, *Fatigue Fract. Eng. M.*, **42**(6), 1341-1356. https://doi.org/10.1111/ffe.12990.

Janeiro, R.P. and Einstein, H.H. (2010), “Experimental study of the cracking behavior of specimens containing inclusions (under uniaxial compression)”, *Int. J. Fract*, **164**(1), 83-102. https://doi.org/10.1007/s10704-010-9457-x.

Jespersen, C., Maclaughlin, M. and Hudyma, N. (2010), “Strength, deformation modulus and failure modes of cubic analog specimens representing macroporous rock”, *Int. J. Rock Mech. Min. Sci.*, **47**(8) 1349-1356. https://doi.org/10.1016/j.ijrmms.2010.08.015.

La, Y.S. and Kim, B. (2020), “Stability evaluation of a double-deck tunnel with diverging section”, *Geomech. Eng.*, **21**(2), 123-132. http://doi.org/10.12989/gae.2020.21.2.123.

Lee, H. and Jeon, S. (2011), “An experimental and numerical study of fracture coalescence in precracked specimens under uniaxial compression”, *Int. J. Solids Struct.*, **48**(6) 979-999. https://doi.org/10.1016/j.ijsolstr.2010.12.001.

Lee, H., Oh, T.M. and Park, C. (2020a), “Analysis of permeability in rock fracture with effective stress at deep depth”, *Geomech. Eng.*, **22**(5), 375-384. http://dx.doi.org/10.12989/gae.2020.22.5.375.

Lee, K.Y., Lee, I.M. and Shin, Y.J. (2020b), “Quantitative assessment of depth and extent of notch brittle failure in deep tunneling using inferential statistical analysis”, *Geomech. Eng.*, **21**(2), 201-206. http://doi.org/10.12989/gae.2020.21.2.201.

Luo, Y. (2020), “Influence of water on mechanical behavior of surrounding rock in hard-rock tunnels: An experimental simulation”, *Eng. Geol.*, **277**, 105816. https://doi.org/10.1016/j.enggeo.2020.105816.

Lotidis, M.A., Nomikos, P.P. and Sofianos, A.I. (2019), “Numerical study of the fracturing process in marble and plaster hollow plate specimens subjected to uniaxial compression”, *Rock Mech. Rock Eng.*, **52**(11), 4361-4386.

https://doi.org/10.1007/s00603-019-01884-8.

Ma, D., Duan, H.Y., Li, W.X., Zhang, J.X., Liu, W.T. and Zhou, Z.L. (2020), "Prediction of water inflow from fault by particle swarm optimization-based modified grey models", *Environ. Sci. Pollut. Res.*, **27**, 42051-42063. https://doi.org/10.1007/s11356-020-10172-w.

Ma, D., Zhang, J.X., Duan, H.Y., Huang, Y.L., Li, M., Sun, Q. and Zhou, N. (2021), "Reutilization of gangue wastes in underground backfilling mining: Overburden aquifer protection", *Chemosphere*, **264**(1), 128400. https://doi.org/10.1016/j.chemosphere.2020.128400.

Martin, C.D. (1993), "Strength of massive Lac du Bonnet granite around underground openings", Ph.D. Dissertation, University of Manitoba, Manitoba, Canada.

Maruvanchery, V. and Kim E. (2020), "Effects of water on rock fracture properties: Studies of mode I fracture toughness, crack propagation velocity, and consumed energy in calcite-cemented sandstone", *Geomech. Eng.*, **17**(1), 57-67. http://dx.doi.org/10.12989/gae.2019.17.1.057.

Mellor, M. and Hawkes, I. (1971), "Measurement of tensile strength by diametral compression of discs and annuli", *Eng. Geol.*, **5**(3), 173-225. https://doi.org/10.1016/0013-7952(71)90001-9.

Peng, L., Wong, R.H.C. and Tang, C.A. (2015), "Experimental study of coalescence mechanisms and failure under uniaxial compression of granite containing multiple holes", *Int. J. Rock Mech. Min. Sci.*, **77**, 313-327. https://doi.org/10.1016/j.ijrmms.2015.04.017.

Sammis, C.G. and Ashby, M.F. (1986), "The failure of brittle porous solids under compressive stress states", *Acta Metall. Sin.*, **34**(3), 511-526. https://doi.org/10.1016/0001-6160(86)90087-8.

Tang, C.A., Wong, R.H.C., Chau, K.T. and Lin, P. (2005), "Modeling of compression-induced splitting failure in heterogeneous brittle porous solids", *Eng. Fract. Mech.*, **72**(4), 597-615. https://doi.org/10.1016/j.engfracmech.2004.04.008.

Tao, M., Ma, A., Cao, W.Z., Li, X.B. and Gong, F.Q. (2017), "Dynamic response of pre-stressed rock with a circular cavity subject to transient loading", *Int. J. Rock Mech. Min. Sci.*, **99**, 1-8. https://doi.org/10.1016/j.ijrmms.2017.09.003.

Tasdemir M.A., Maji, A.K. and Shah S.P. (1990), "Crack propagation in concrete under compression", *J. Eng. Mech.*, **116**(5), 1058-1076. https://doi.org/10.1061/(ASCE)0733-9399(1990)116:5(1058).

Ulusay, R. and Hudson, J.A. (2007), *The Complete ISRM Suggested Methods for Rock Characterization, Testing and Monitoring: 1974-2006*, ISRM Turkish National Group, Ankara, Turkey.

Wagner, H. (2019), "Deep mining: A rock engineering challenge", *Rock Mech. Rock Eng.*, **52**(5), 1417-1446. https://doi.org/10.1007/s00603-019-01799-4.

Wang, S.H., Lee, C.I., Ranjith, P.G. and Tang, C.A. (2009), "Modeling the effects of heterogeneity and anisotropy on the excavation damaged/disturbed zone (EDZ)", *Rock Mech. Rock Eng.*, **42**, 229-258. https://doi.org/10.1007/s00603-009-0177-3.

Wang, S.Y., Sloan, S.W., Sheng, D.C. and Tang, C.A. (2012), "Numerical analysis of the failure process around a circular opening in rock", *Comput. Geotech.*, **39**, 8-16. https://doi.org/10.1016/j.compgeo.2011.08.004.

Wang, S.Y., Sun, L., Yang, C.H., Yang, S.Q. and Tang, C.A. (2013), "Numerical study on static and dynamic fracture evolution around rock cavities", *J. Rock Mech. Geotech. Eng.*, **5**(4), 262-276. https://doi.org/10.1016/j.jrmge.2012.10.003.

Weng, L., Li, X.B., Shang, X.Y. and Xie, X.F. (2018), "Fracturing behavior and failure in hollowed granite rock with static compression and coupled static-dynamic loads", *Int. J. Geomech.*, **18**(6), 04018045. https://doi.org/10.1061/(ASCE)GM.1943-5622.0001132.

Wennberg, O.P., Rennan, L. and Basquet, R. (2009), "Computed tomography scan imaging of natural open fractures in a porous rock; geometry and fluid flow", *Geophys. Prospect.*, **57**(2), 239-249. https://doi.org/10.1111/j.1365-2478.2009.00784.x.

Westphal, H., Surholt, I., Kiesl, C., Thern, H.F. and Kruspe, T. (2005), "NMR measurements in carbonate rocks: Problems and an approach to a solution", *Pure Appl. Geophys.*, **162**, 549-570. https://doi.org/10.1007/s00024-004-2621-3.

Wong, R.H.C., Lin, P. and Tang, C.A. (2006), "Experimental and numerical study on splitting failure of brittle solids containing single pore under uniaxial compression", *Mech. Mater.*, **38**(1-2), 142-159. https://doi.org/10.1016/j.mechmat.2005.05.017.

Wu, H., Kulatilake, P.H.S.W., Zhao, G.Y., Liang, W.Z. and Wang, E.J. (2019), "A comprehensive study of fracture evolution of brittle rock containing an horseshoe-shaped cavity under uniaxial compression", *Comput. Geotech.*, **116**, 103219. https://doi.org/10.1016/j.compgeo.2019.103219.

Wu, H., Zhao, G.Y. and Liang, W.Z. (2019), "Mechanical response and fracture behavior of brittle rocks containing two horseshoe-shaped holes under uniaxial loading", *Appl. Sci.*, **9**(24), 5327. https://doi.org/10.3390/app9245327.

Wu, H., Zhao, G.Y. and Liang, W.Z. (2020), "Mechanical properties and fracture characteristics of pre-holed rocks subjected to uniaxial loading: A comparative analysis of five hole shapes", *Theor. Appl. Fract. Mec.*, **105**, 102433. https://doi.org/10.1016/j.tafmec.2019.102433.

Wu, H., Zhao, G.Y. and Liang, W.Z. (2019), "Investigation of cracking behavior and mechanism of sandstone specimens with a hole under compression", *Int. J. Mech. Sci.*, **163**, 105084. https://doi.org/10.1016/j.ijmecsci.2019.105084.

Wu, Y.H., Cheng, L.S., Killough, J., Huang, S.J., Fang, S.D., Jia, P., Cao, R.Y. and Xue, Y.C. (2021), "Integrated characterization of the fracture network in fractured shale gas Reservoirs—Stochastic fracture modeling, simulation and assisted history matching", *J. Petrol. Sci. Eng.*, **205**, 108886. https://doi.org/10.1016/j.petrol.2021.108886.

Yamaguchi, I. (1981), "A laser-speckle strain gauge", *J. Phys. E Sci. Instrum.*, **14**(11), 1270-1273. https://doi.org/10.1088/0022-3735/14/11/012.

Zeng, W., Yang, S.Q. and Tian, W.L. (2018), "Experimental and numerical investigation of brittle sandstone specimens containing different shapes of holes under uniaxial compression", *Eng. Fract. Mech.*, **200**, 430-450. https://doi.org/10.1016/j.engfracmech.2018.08.016.

Zhu, W.C., Liu, J.S., Tang, C.A., Zhao, X.D. and Brady, B.H. (2005), "Simulation of progressive fracturing processes around underground excavations under biaxial compression", *Tunn. Undergr. Sp. Tech.*, **20**(3), 231-247. https://doi.org/10.1016/j.tust.2004.08.008.

Zakharov, E.V. and Kurilko, A.S. (2014), "Effects of low temperatures on strength and power input into rock failure", *Sci. Cold Arid Reg.*, **6**(5), 0455-0460. https://doi.org/10.3724/SP.J.1226.2014.00455.

Zerhouny, M., Fadil, A. and Hakdaoui, M. (2018) "Underground space utilization in the urban land-use planning of Casablanca (Morocco)", *Land*, **7**(4), 143. https://doi.org/10.3390/land7040143.

CC